Daily dust variation from the PFS MEx observations

by

Paulina Wolkenberg[1], Marco Giuranna[1]

[1] Istituto di Astrofisica e Planetologia Spaziali – Istituto Nazionale di Astrofisica (IAPS – INAF) via del Fosso del Cavaliere, 100, 00133 Roma, Italia

Corresponding author:

Paulina Wolkenberg

IAPS – INAF

Via del Fosso del Cavaliere 100

Rome, 00133, Italy

e-mail: paulina.wolkenberg@inaf.it, pwolkenberg@gmail.com

Abstract

We collected over 7 Martian years (MY) of data observed by the Planetary Fourier Spectrometer (PFS) to present a daily variation of dust content in the Martian atmosphere. We found three typical behaviors of dust opacities with LT (local time). The most peculiar variation was observed when global dust storms (MYs 28 and 34) or particularly strong regional storms (MY 29) occurred on Mars. Here, large dust opacities were measured at 10 LT (MY 34) and 11 LT (MY 28). Then, relatively small values of dust opacities were found in the evening (20 LT). The non-dusty season, particularly near northern summer solstice, was characterized by a deep minimum of the total dust opacity at late night/early morning, while small variations around the mean value were observed during daytime. The clear trend of dust was observed over both hemispheres during early morning. We noted elevated dust opacities in the second half of the year compared to the non-dusty season in all Martian years without global dust storms. The daily variation of three types of storms occurring in moderately dusty conditions was also investigated. Dust in A storms was present in the atmosphere at all LTs and was mostly confined to the southern hemisphere. The maximum of dust opacities in B storms was found at 15 – 17 LT, close to the South Pole. C storms were mainly constrained to southern latitudes and occurred from the late morning to midday.

1. Introduction

Thanks to elliptical orbits by the Mars Express spacecraft (MEx), Planetary Fourier Spectrometer (PFS) is able to investigate a daily cycle of atmospheric components such as dust or water-ice. Dust is a strongly variable constituent of the Martian atmosphere. A seasonal variation of dust with L_s (solar longitude) has been widely documented, based on data acquired from past and present missions: Viking (Martin et al., 1979), Mariner 9 (Santee and Crisp, 1993; Fenton et al., 1997), Mars Global Surveyor (Smith, 2004), Mars Odyssey (Smith, 2009), Mars Reconnaissance Orbiter (McCleese et al., 2010; Kass et al., 2016), and Mars Express (Zasova and Formisano, 2007; Määttänen et al., 2013). The spatial and seasonal behavior of dust in the atmosphere depends on the occurrence of global dust storms (Haberle, 1986). Based on the analysis of 4 years of pressure, temperature and wind from the Viking meteorological station by Leovy et al. (1985), Haberle (1986) found that the weather on Mars was governed by two different regimes during southern summers. The first regime was associated with the occurrences of global dust storms in which dust was transported from the southern hemisphere by a cross-equator Hadley circulation (Haberle, 1986). Near perihelion, over the southern subtropics, insolation was strong and mean upward vertical atmospheric motions dominated (Haberle, 1986). In years without the global dust storms, in the second regime, dust was lifted from the northern hemisphere by relatively active mid-latitude storm systems (Haberle, 1986). From numerical simulations when the northern dust haze diminished, its contribution to the surface stress decreased in the southern hemisphere and prevented the development of a global dust storm (Haberle, 1986). The two circulations in the opposite hemispheres compete between each other (Haberle, 1986), and as a result they could give some indications about when a global dust storm occurs. For example, stronger southern circulation favored the occurrence of a global dust storm. However, the origin of global dust storms is still unknown.

PFS is the instrument which enables observations of the diurnal variation of suspended dust. Previous missions had a limited coverage of local times. However, some analysis at the variation of dust opacity during daytime from the IRTM (Infrared Thermal Mapper) Viking measurements was presented by Martin and Tamparri (2007). They found that dust increased in the atmosphere at 10 - 12 LT and then gradually decreased in the late afternoon around 16 LT. The MCS (Mars Climate Sounder) MRO (Mars Reconnaissance Orbiter) instrument also detected a diurnal variation of dust opacity around the northern summer solstice over the northern tropics (Heavens et al., 2011). The high altitude dust maximum (HATDM) varied 3 times over the course of a 24-hour day (Fig.2b, d in Heavens et al., 2011, Heavens et al., 2014). Recently, MCS vertical dust distributions during the global dust storm in MY 34 showed differences between day and night (Kleinboehl et al., 2020). These differences depended on the fact that the vertical extent of dust was higher during day than night, especially during a mature phase of the global dust storm. The top altitude of the dust changed over the course of the 24-hour day particularly at the high southern latitudes (Kleinboehl et al., 2020). This means that the total dust amount in the atmosphere varies during a 24-hour day.

This daily cycle of dust is still poorly understood, and we are trying to answer the question of how long dust is suspended in the atmosphere. The current climate models are still doing very poorly to simulate diurnal variation in the dust distribution. More analysis and comparison to the current GCMs (global circulation models) are needed for a complete interpretation of PFS observations.

Dust can be investigated indirectly by observing brightness temperatures at 15 μm and atmospheric temperatures at 25 km (0.5 mb). The brightness temperatures allow us to study a deep layer of the atmosphere centered at roughly 0.5 mb, corresponding to an elevation of 25 km (Wilson and Richardson, 2000). A significant seasonal variation of the global mean temperature was found by Leovy (1985) and Clancy et al. (1996) due to a large seasonal modulation in atmospheric dust content (Zurek et al., 1992). Global brightness temperatures at 15 μm rapidly rose up along with the onset of each of the two 1977 global dust storms (Wilson and Richardson, 2000). These brightness temperature increases were due to a direct heating of the atmosphere by dust (Wilson and Richardson, 2000). Aerosol affected atmospheric temperatures leading to diurnal variations presented by Wilson and Richardson (2000). Data from Mariner 9 Infrared Interferometer Spectrometer (IRIS) during the 1971 global dust storm revealed the 30 K difference (peak-to-peak), extending to at least 40 km (Hanel et al., 1972). The similar diurnal temperature variations at 25 km were observed in the IRTM brightness temperatures at 15 μm when the onset of two global dust storms occurred (1977a and 1977b) (Martin and Kieffer 1979).

In this work, we present three typical daily variations of dust opacities observed by PFS in non- and dusty seasons. The zonally averaged dust as a function of latitude and LT is illustrated. We characterize the LT variation of seasonal types of storms defined by Kass et al. (2016).

2. Typical behaviors of dust activity with LT

Dust opacities are obtained from PFS radiance measurements in a spectral range around 1075 cm^{-1} (9.3 μm) where the dust absorption band is observed. In our analysis we also use vertical temperature profiles retrieved from radiance measurements performed in a spectral range corresponding to the main CO_2 absorption band at 667 cm^{-1} (15 µm). All retrieved parameters with surface temperatures are obtained using the optimal estimation method with the Bayesian approach (Grassi et al., 2005).

The error analysis presented in Wolkenberg et al. (2018) showed that the mean values of uncertainties for dust opacities were 0.06 and 0.11 for surface temperatures greater than 220 K and less than 220 K, respectively. In this study, a dataset of ~ 5000 selected retrievals of dust opacity, spanning all combinations of Ls, LT and location was gathered to demonstrate a histogram of dust opacity standard deviations as a function of LT. The same retrievals were applied in Wolkenberg et al. (2018) and collected from MY 28. Standard deviations of dust opacity vary with LT within 0.06 – 0.13 (Fig.1a, b). We obtained a similar result for two populations of surface temperatures greater than and less than 220 K, respectively. The maximum values are observed from 4 LT to 8 LT and then the standard deviation progressively decreases with LT down to 0.05 (Fig.1b).

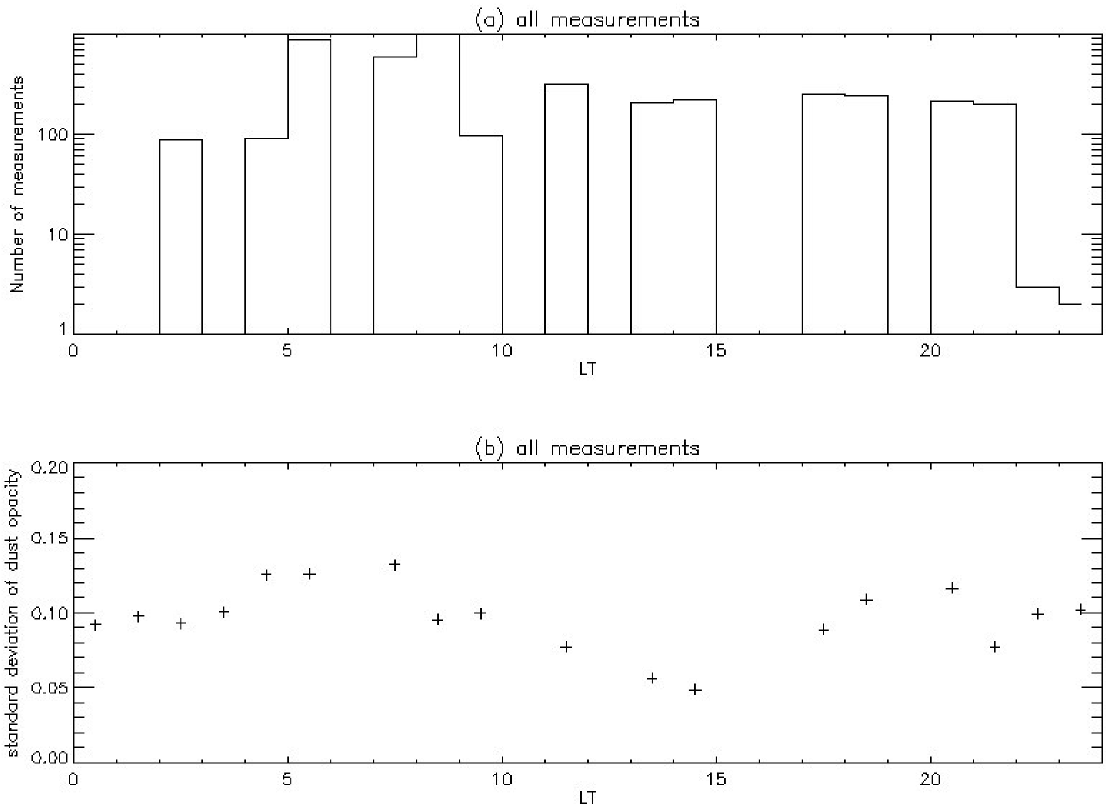

Fig. 1. Histogram of standard deviations for dust opacity: (a) number of measurements as a function of LT, (b) standard deviations of dust opacity as a function of LT. Gaps in Fig.1b mean no measurements.

As expected, large standard deviations occur during the night and early morning when surface temperatures are less than 220 K. They then gradually decrease to around 0.05 with surface temperatures larger than 220 K and again reach a large value in the evening. The largest values of standard deviations are encountered during rapid changes of insolation in the early morning, 5 - 7 LT, and in the evening, 18 – 20 LT. We also investigated the seasonal variation of dust opacity standard deviations. Fig.2 presents a histogram of standard deviations as a function of season (L_s).

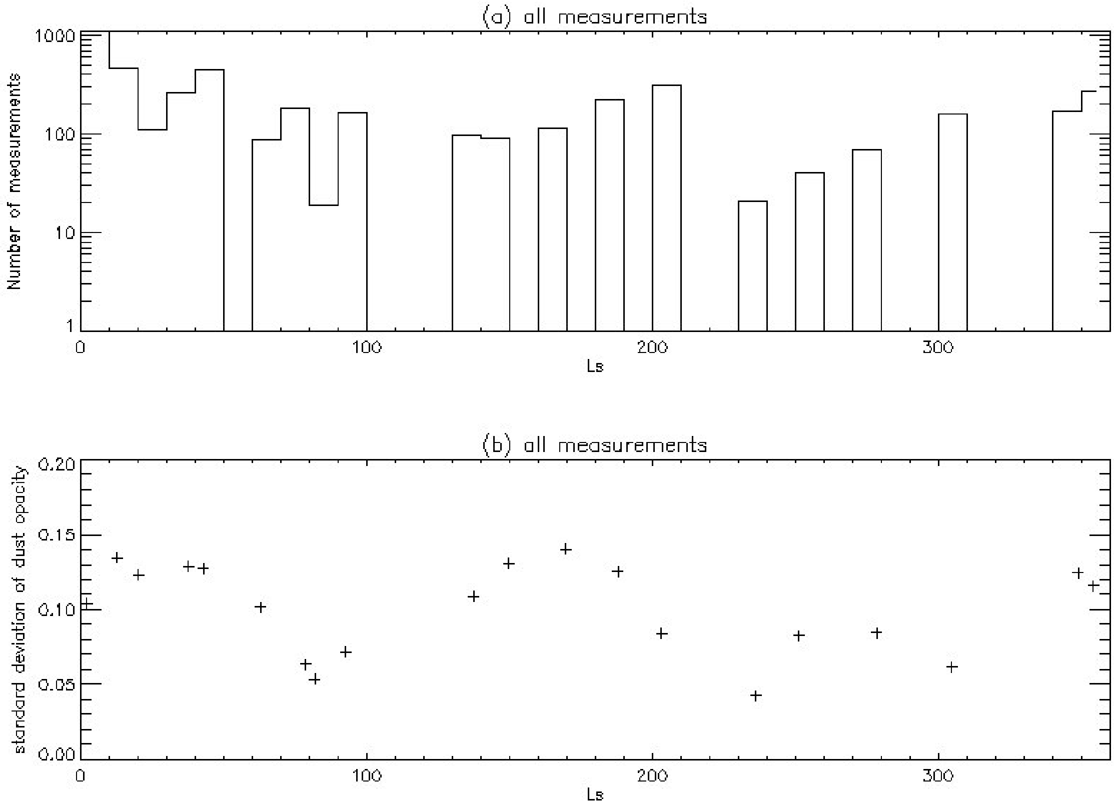

Fig.2. Histogram of standard deviations for dust opacity, (a) number of measurements as a function of L_s, (b) standard deviations of dust opacity as a function of L_s. Gaps in Fig.2b mean no measurements.

The seasonal variation of dust opacity standard deviations is different than for LT. We observe almost two minima of standard deviations of dust opacity at around $L_s = 80°$ and $L_s = 230°$. The two minima coincide approximately with the aphelion and perihelion seasons. The largest standard deviations are found at the beginning of the year at $L_s = 10°$ to 40° then from 140° to 180° and from 350° – 360°. Thus the maxima coincide with the equinox seasons. However, standard deviations are within 0.04 – 0.14 during the whole year, consistent with results by Wolkenberg et al. (2018).

We also performed tests on sensitivity of retrieval for column integrated dust opacities using the different vertical dust distributions as an 'a priori' profile. The results of total dust opacities were compared with the original obtained by using vertical dust distributions derived from the EMCD v4.2 database (Forget et al., 1999a,b) and derived from an analytical formula given by Heavens et al. (2011, eq.15). We find a negligible effect of different vertical distributions on retrieved total dust opacities during daytime and nighttime. We only observe a relative difference of 10% in the total dust opacities (for example 1.72 vs. 1.52) when high dust loadings occur in the atmosphere. A detailed analysis can be found in Appendix A.

2.1. Diurnal dust activity during global dust storms in MY 28 and MY 34 and the regional dust storm in MY 29

Fig.3 presents seasonal variations of zonal mean dust opacities averaged for a region from 40.5°S to 40.5°N. The most striking features are very large dust opacities during dusty seasons in MY 28 and MY 34. Moderate–to-large dust activities are also observed a year before and after MY 28 and a year before MY 34. The regional, planet-encircling dust storm observed in MY 29 had a moderate–to-large dust opacity around 0.5. Dust opacities around 0.3 are observed in dusty seasons of other years. After an analysis of dust activity from L_s = 331° of MY 26 to L_s = 300° of MY 34, we selected data for intervals when the global dust storms occurred (i.e. in MY 28 and MY 34).

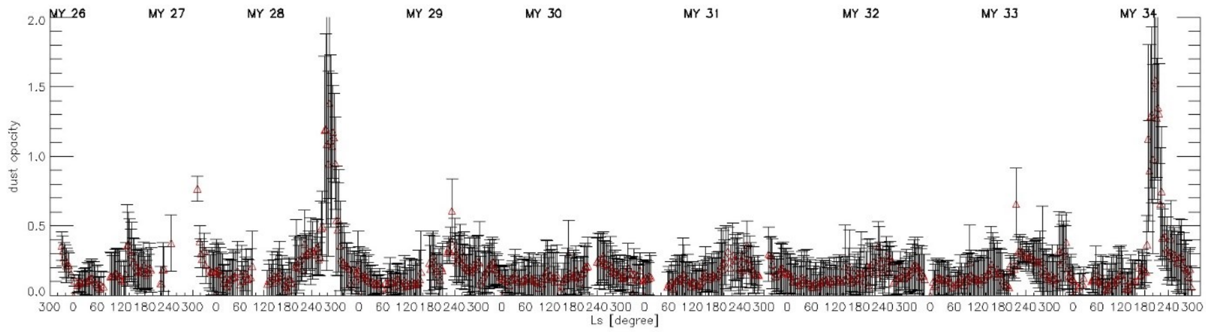

Fig.3. Zonal mean dust opacity averaged for a region from 40.5°S to 40.5°N as a function of L_s. The data are binned in L_s of 3°. Dust opacity is normalized to the reference pressure 6.1 mbar. Standard deviations contain variabilities of dust opacity within each bin. An "error bar" represents the standard deviation of each averaged value and provide an indication of the observed zonal and meridional variations.

Data was separated based on the particular behavior, which was not observed in the other MYs, of dust opacities with LT in MY 28, MY 29 and MY 34.

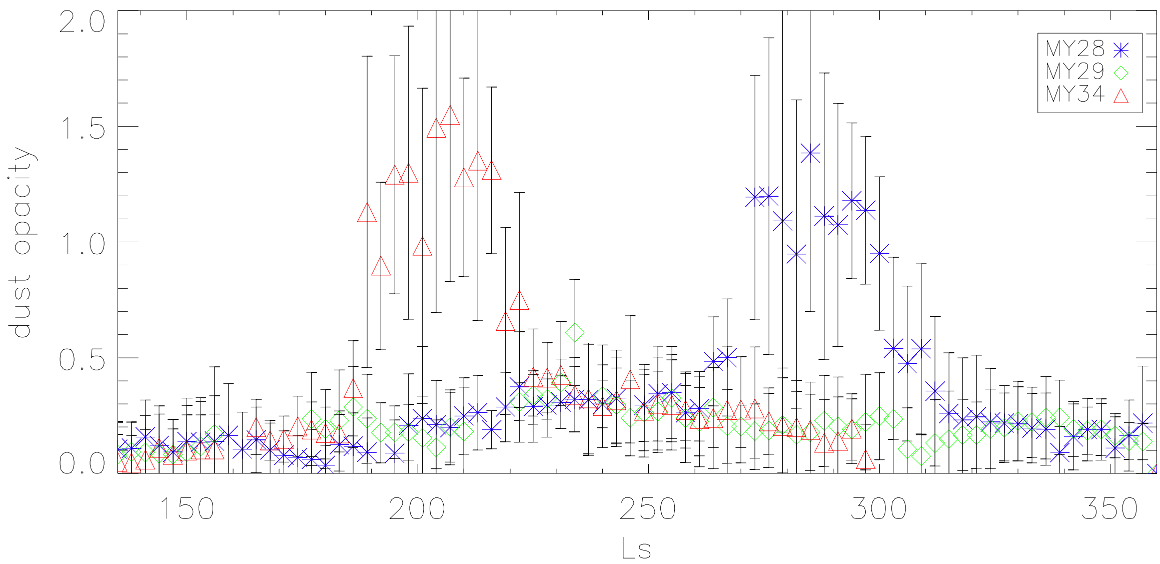

Fig.4. Zonal mean dust opacities averaged for the region from 40.5°S to 40.5°N in MY 28, 29 and 34. The data are binned in L_s of 3°. Dust opacities are normalized to the reference pressure 6.1 mbar. Standard deviations contain variabilities of dust opacity within bin. The "error bars" represent the standard deviation of each averaged value and provide an indication of the observed zonal and meridional variations.

We also analyzed the northern and southern hemispheres within 40.5°N and 40.5°S latitudes, respectively. The evolution of global dust storms and the regional dust storm in MY 29 during L_s = 135° - 360° are plotted in **Fig.4**. We distinguish the onset, core and decay phases in each global storm. Each storm starts at a different L_s. For example, in MY 34, the storm begins at L_s =190° and its core has a duration of 30° L_s approximately (**Fig.4**). The MY29 regional storm starts as a flushing storm around Ls=230, peaking at Ls=238 as it spreads southward and westward. It gradually decays afterwards. The global dust storm in MY 28 starts later in the year, at L_s = 262°, and continues until L_s = 311°.

Our main purpose was to show a variation of dust content during daytime and nighttime for high dust activity periods (global dust storms). We plotted dust opacities as a function of LT and Ls during the storms for each year considered (**Fig.5**).

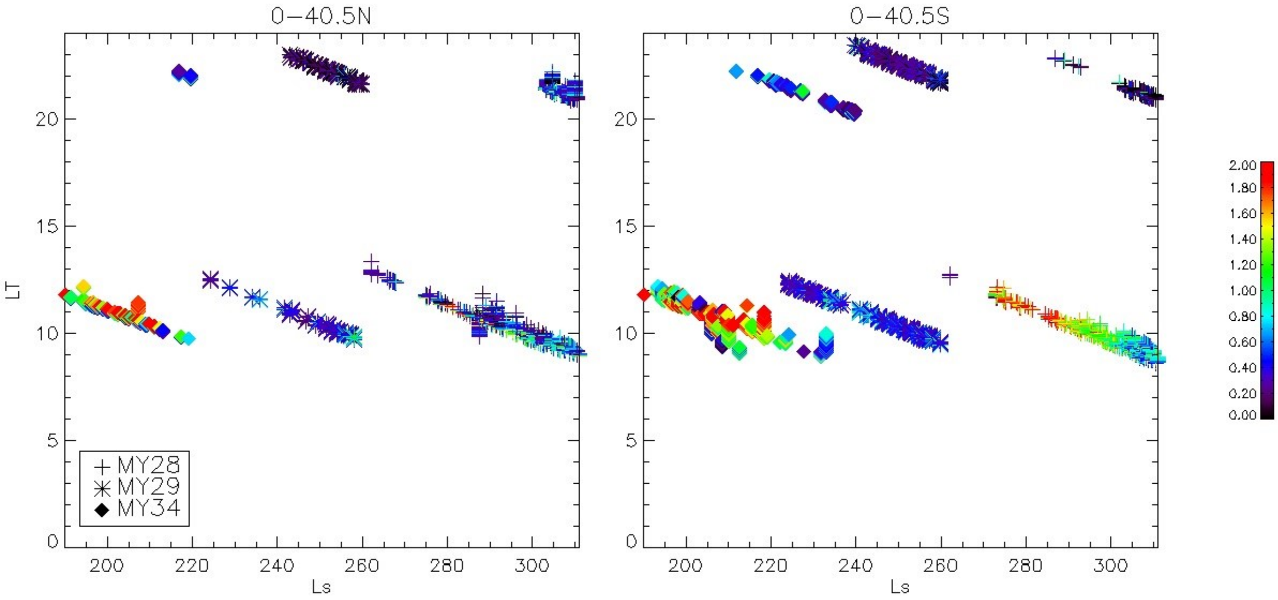

Fig.5. Dust opacities as a function of LT and Ls for the northern hemisphere (left panel) and the southern hemisphere (right panel) during global storms in MY 28 and 34 and the regional storm in MY 29. Some values of dust opacities can exceed 2.

All column-integrated dust opacities retrieved by PFS are presented separately for the northern (0-40.5°N) and the southern (0-40.5°S) hemispheres (Fig.5). The most spectacular behavior of dust is observed before midday in MY 28 and MY 34 in **Fig.5**. The elevated dust opacity is found between 10 – 12 LT in MY 28 and MY34. We note lower values of dust opacities in the evening/early night compared to the dust content before midday for all considered years. Unfortunately, in MY 28 and MY 34 in the northern hemisphere our observations of the evening/early night dust opacities occurred during a decay phase of the dust storms. Moreover, the contrast, in both years, between midday and early night observations is smaller in the northern than southern hemisphere: in the core of the MY 28 storm and at the beginning of the decay phase at Ls ~ 285, the gap in daytime and nighttime activity is more distinct in the southern hemisphere, even late in the decay phase. During the core of the dust storm in MY 34, dust opacities are measured from 9 - 12 LT over the southern hemisphere. Smaller dust opacities are found at 9 LT compared to values at 10 and 11 LT at around Ls = 210. Similarly to the MY28 storm, we observe dust opacities in the late evening at the end of the storm core and at the beginning of the decay phase. The contrast between midday and late evening observations is greatly pronounced until Ls = 220. This contrast decreases gradually with the progressing season. The regional dust storm in MY 29 shows less contrast between midday and late evening measurements for both hemispheres.

To better analyze the LT variation excluding the seasonal effect we made figures with L_s bin equal to 1° during the L_s range of large dust opacities. **Fig.6** presents dust opacities as a function of LT for some sols in MY 28. We have binned the data by 1° in Ls, by 3° in latitude and by 1 hour. Then we averaged the binned data from 40.5°S to the equator and from the equator to 40.5°N. For our example we took the southern latitude range because the storm core mostly appeared over this region. Dust opacities available at different LTs were set into groups with similar behaviors. At 11 - 12 LT, dust opacities show a large range of values between 1.3 – 2.5, from Ls = 273 to Ls = 281 (first group). The maximum values of dust opacities are observed at 11 - 12 LT in our dataset at around L_s = 281°. We also note that dust opacities increase progressively within the first group at 11-12 LT, but this is due to a seasonal effect.

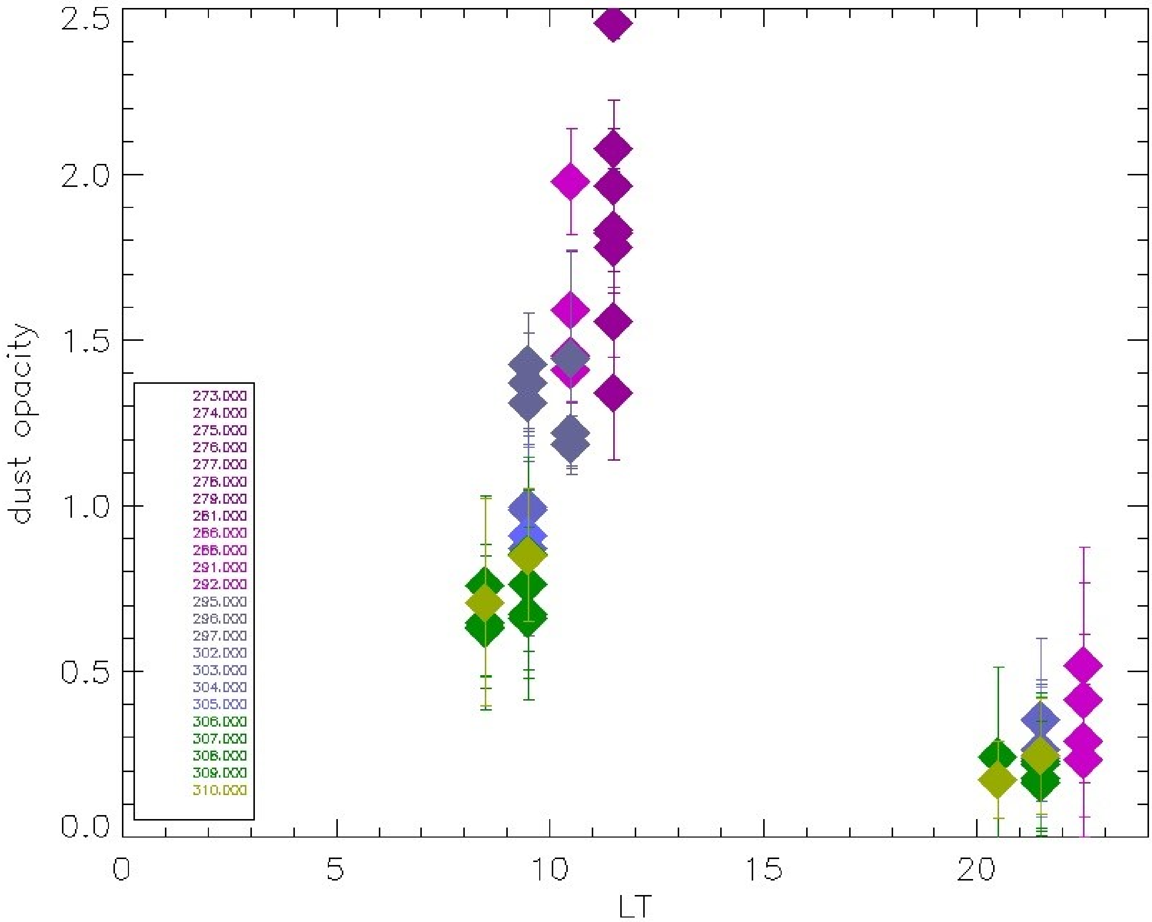

Fig.6. Dust opacities as a function of LT for L_s bin (1°) shown in the legend in MY 28 for the southern hemisphere (0 – 40.5°S). Some gaps are evident in L_s bins. The “error bars” represent the standard deviation of each averaged value and provide an indication of the observed zonal and meridional variations. As expected, such variations are particularly large during a global dust storm.

The second group is characterized by the largest differences in dust opacities at 10 - 11 LT and 22 – 23 LT. This group contains observations in the core of this storm and at the beginning of the decay phase from Ls = 286 to Ls = 292. The next group is from Ls = 295 to Ls = 297. Within this group, observations are taken only in the morning from 9 to 11 LT and show 1.2 – 1.5 of dust opacities. In the decay phase, from Ls = 302 to Ls = 304, the differences in dust opacities are observed between the morning (9 – 10LT) and the evening (21 – 22 LT). The differences then gradually diminish but they are still evident even at L_s = 310°. There are several gaps in L_s bins but it is clear that dust opacities from 8 – 11 LT are larger than in the evening at around 20 – 22 LT. The most interesting behavior is found at 9 LT when the dust opacities vary from 0.4 to 1.4 during most available later L_s bins (295° – 310°). Dust opacity starts changing from 1.4 at L_s = 295° and gradually decreases with season at this LT. Unfortunately, we are not able to claim that dust activity grows with LT for each day during morning hours. We observe a seasonal effect. Only observations at L_s = 310° show dust increasing from 8 to 9 LT and the difference in dust opacities between morning and evening hours. In **Fig.6** dust opacities at LT 12 are not plotted because not enough measurements were taken during the onset of the storm for L_s < 273 (Fig.5).

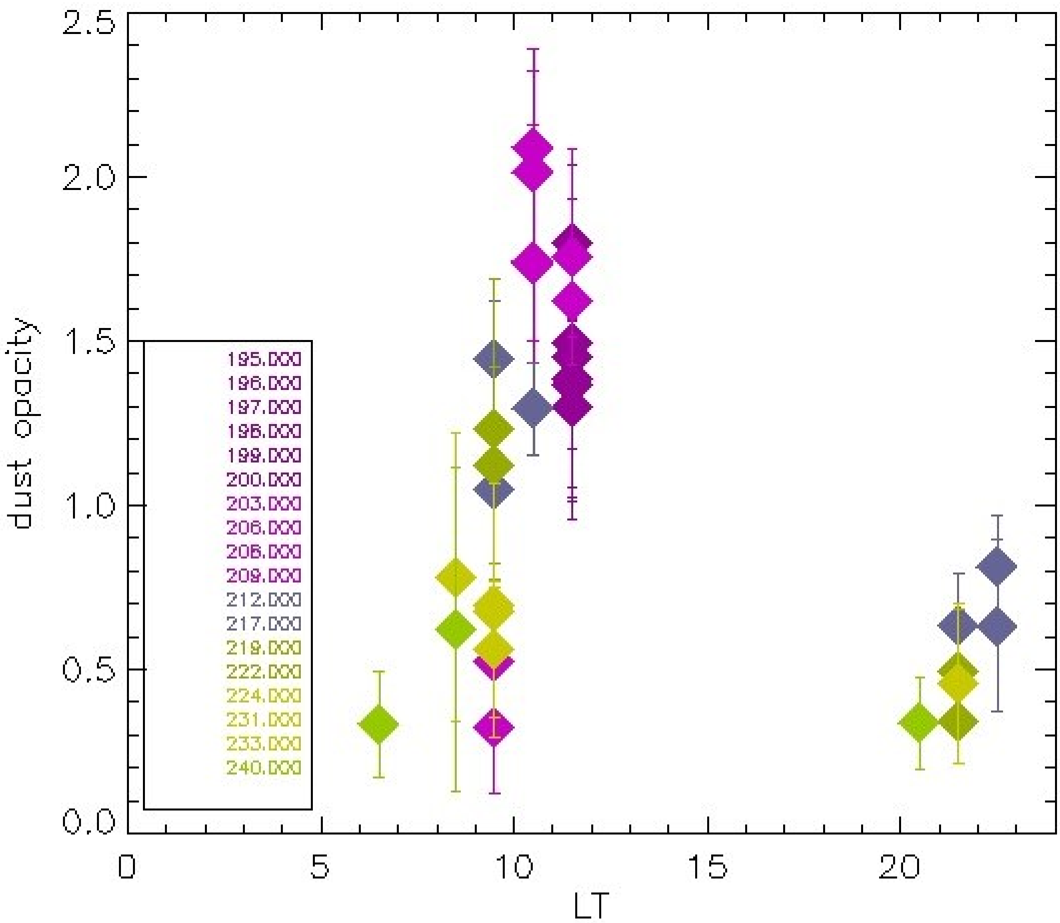

Fig.7. Dust opacities as a function of LT for different Ls bins shown in the legend in MY 34 for the southern hemisphere (0 – 40.5°S). The "error bars" represent the standard deviation of each averaged value and provide an indication of the observed zonal and meridional variations. As expected, such variations are particularly large during a global dust storm.

Fig. 7 shows a similar behavior of dust opacities as a function of LT for the core and the decay phase of storm in MY 34. However, some differences are observed with respect to MY 28. In MY 34, the maximum is observed at 10 - 11 LT. Observations at 11 - 12 LT show small decreases of dust opacities with respect to values at 10 LT. Contemporaneously these observations at 11 - 12 LT show a variation with season from L_s = 195° to 200°. There is then a gap at larger L_s for this LT. At L_s = 203° – 209° we also observe the dust increasing from 9 to 10 LT. Also, the dust activity at 9 LT grows with season in the core of the dust storm and decreases, for example, at L_s = 233° (lightest green points). As in the case of MY 28, we observe again a large difference in dust opacities between 9 - 10 LT and in the evening during the L_s interval from 212° to 222°. However, the diurnal differences are also present in the decay stage of the storm, at a time when active dust lifting is almost certainly less pronounced. Dust opacities are within 1.3 – 1.4 in the morning (9 – 10 LT), whereas in the evening 21 – 22 LT we find still large values but less than 0.7 (L_s = 212° – 231°). Finally, at the end of the storm (decay phase) at L_s = 231° we still observe differences between morning and evening hours, but these differences decrease gradually to achieve a very similar level during the whole day.

Here we note a strong correlation between surface wind stress and the observed daily variation of dust opacity during the global dust storm of MY28. In **Fig. 8a** we show the zonally averaged surface wind stress as a function of local time for the southern hemisphere (0-60° S latitude) as inferred from the MCD v5.3 (Millour et al., 2015; Forget et al, 1999a,b). We use the MY 28 scenario, which corresponds to the best representation by the model of this specific year, both in terms of daily atmospheric dust loading and daily solar EUV (Extreme Ultraviolet scenario) input. Solar longitude is L_s = 270° (southern summer solstice), which is during the onset of the MY 28 global dust storm (**Fig. 3 and 4**). The surface wind stress shows a strong temporal (LT) and latitudinal dependence. Similar to dust, it rapidly increases after 6 LT and the largest values are observed between 8 LT and 12 LT, with a peak around 10 LT (Fig.8b). Then, it rapidly decreases until 15 LT and stays low afterwards. The surface wind stress is maximum around the sub-solar latitudes, between 20° and 30° S (**Fig. 8a**). Newman et al. (2002) find a threshold-dependence for wind stress lifting to reproduce Martian dust storms. With this feature applied, sharp increases in opacity could be produced upon dust storm initiation, as observed. Moreover, these authors also note an important feedback effect for wind stress lifting. Dust raised from the surface heats the near-surface atmosphere forming the temperature gradient which strengthens low-level winds, and thus encourages further lifting.

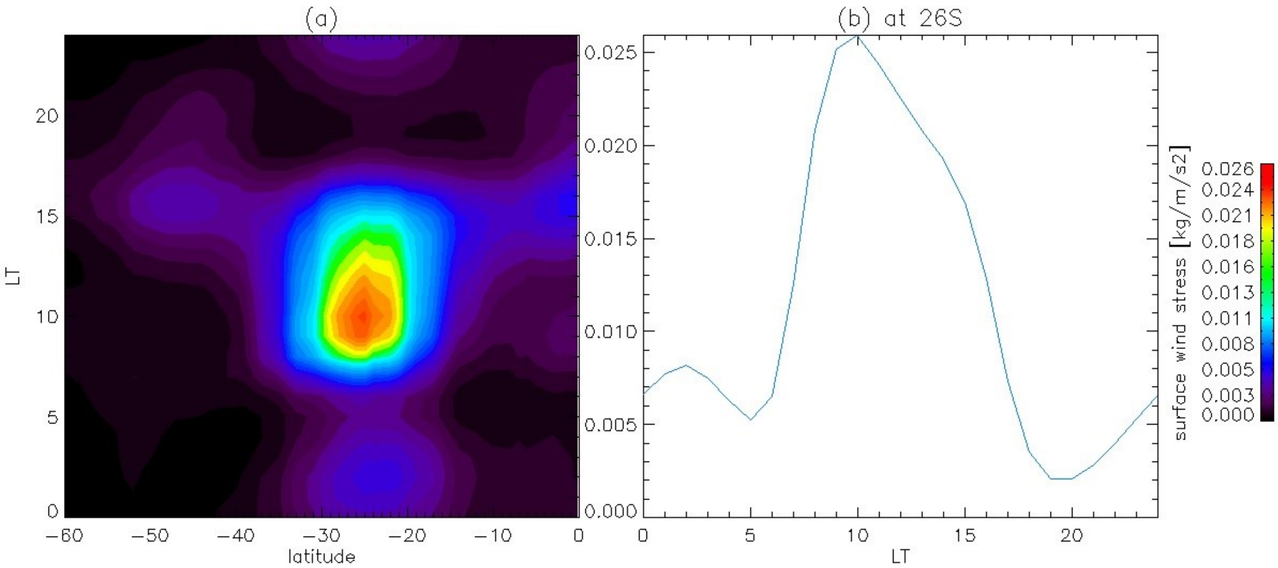

Fig. 8. Zonally averaged surface wind stress at the southern summer solstice as a function of local time, as inferred from the MCD v5.3 using the Mars Year 28 scenario (a) for the latitudinal range 0-60°S latitude, and (b) at 26°S latitude.

As a consequence, lifting via near-surface wind stress is an explosive process, making it a suitable candidate for the rapid injection of dust that is observed by PFS.

2.2. Dust in typical Martian year (dusty season). Storms A, B and C in PFS results as a function of latitude and LT.

Contrary to the dust increase observed during strong dust activity in MY 28, MY 29 and MY 34, we find no special trend in variation of dust opacity with LT in the dusty season for a typical Martian year. We will call the typical Martian year the year of all MYs combined together, observed by PFS, except for MY 28, MY 29 and MY 34. The peculiar behavior with the large increase of dust opacity before midday is not observed in other MYs during the dusty season.

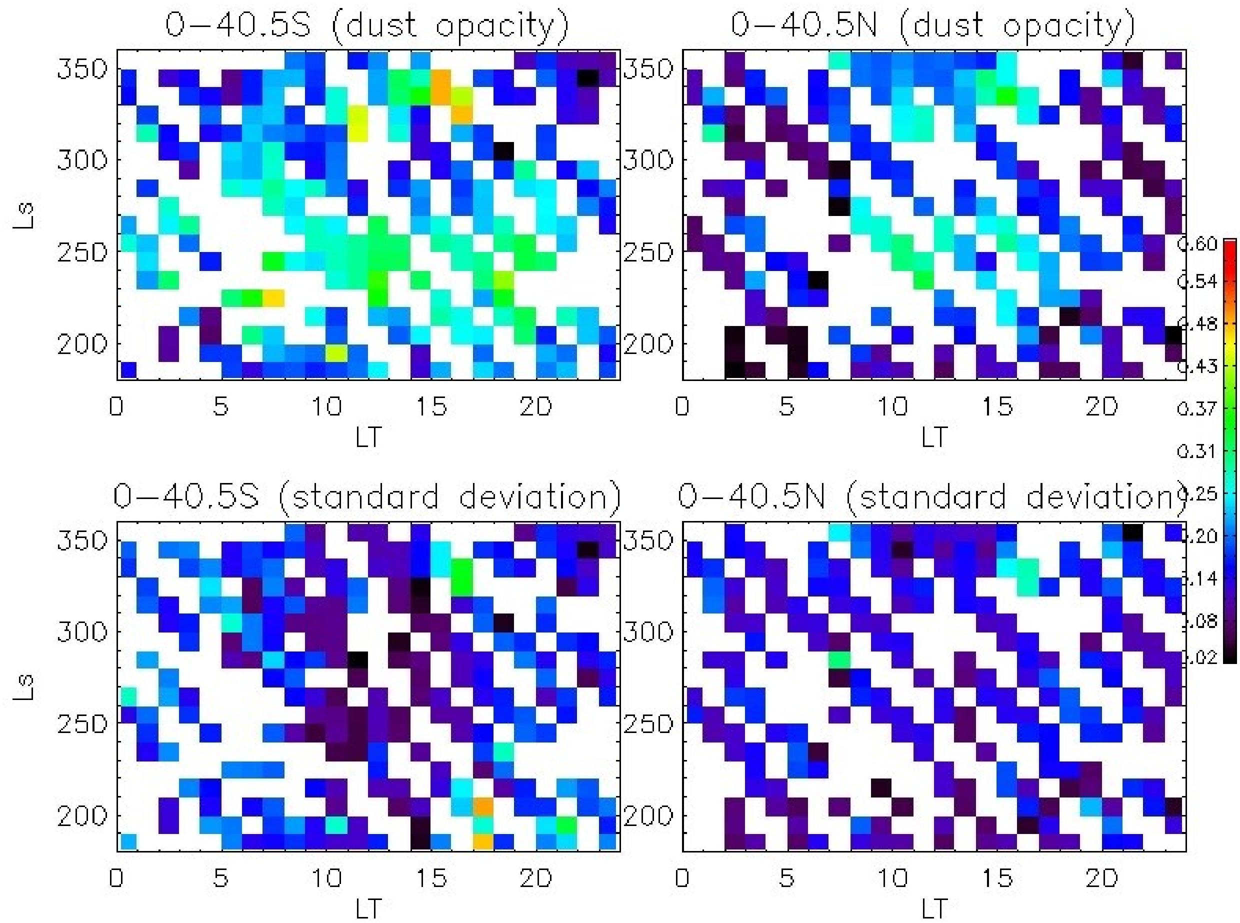

Fig. 9. Dust distribution as a function of solar longitude (Ls) from 180° to 360° and LT for southern hemisphere (0 – 40.5°S) left and for northern hemisphere (0 – 40.5°N) right in typical MY.

Fig. 9 presents the distribution of measurements as a function of L_s and LT for dust opacity with standard deviations within each bin. Bins of 10° of L_s and 1 hour were used in the plot. The difference in dust opacity between daytime and nighttime is more visible in the northern than in the southern hemisphere (**Fig.9**), especially in the L_s range from 220° - 270°. We observe a clear growth in dust opacities with sunrise and decrease with sunset. The next seasonal increase of dust opacities is observed in the L_s range 310° - 350°, in the southern as well in the northern hemisphere. At the beginning of this L_s interval moderate dust opacities around 0.45 occur between 11 – 12 LT in the southern hemisphere, and in the northern hemisphere relatively less. With season the dust activity is shifted toward later hours (15 – 17 LT) in both hemispheres. The seasonal variations of dust were studied in terms of atmospheric temperatures at 0.5 mbar from the MCS MRO observations (Kass et al., 2016). Using this dataset, they defined three types of dust storms (A, B and C), which are recognized in seasonal variations of PFS dust opacities (Wolkenberg et al., 2018). We find similarities to seasonal types of storms defined by Kass et al. (2016). Our purpose in this section is to present some characteristic features of these storm types with LT illustrated also in **Fig. 9** for the typical Martian year. In our results (**Fig.9**) A and B storms are overlapped or combined in one storm starting from around L_s 220° to 270°. The duration of C storms is longer in our results than in MCS observations. The end of C storms is observed at L_s = 350° (**Fig.9**). To compare better our results with MCS observations we plotted the dust variations with LT for L_s intervals when these three types of storms took place (**Fig. 10a, b, c**). **Fig. 10a** presents the dust opacities during the L_s interval corresponding with the duration of A storms (210° – 240°). Dust in A storms occurs at all LTs and is mostly confined to the southern hemisphere. There are no special regions and time of day when dust is pronounced. We found less dust in the northern hemisphere up to 50°N than in the southern hemisphere. This amount in the northern hemisphere decreases from midday to around 16 LT.

Fig. 10b illustrates the behavior of B storms with LT for the L_s range from 240° to 280°. The elevated dust opacity is evident over southern polar regions during daytime and nighttime. The maximum of the dust opacities (around 0.7) is found at 15 – 17 LT, close to the South Pole which is consistent with **Fig. 1** in Kass et al. (2016). In **Fig.1** in Kass et al. (2016) B storms start at the end of A storms. The decay phase of the A storms is observed in the B storms between 9 and 12 LT. The storm's moderate dust activity (0.4) is found over southern and mid-northern latitudes. This dust opacity maximum in B storms is similar to the increase at 10 – 12 LT for the strong dust activity in MY 28 and MY 34 in **Fig. 5, 6, 7**. A relatively clear atmosphere is observed over latitudes from 30°N to 60°N. This non-dusty condition continues from the late afternoon until night.

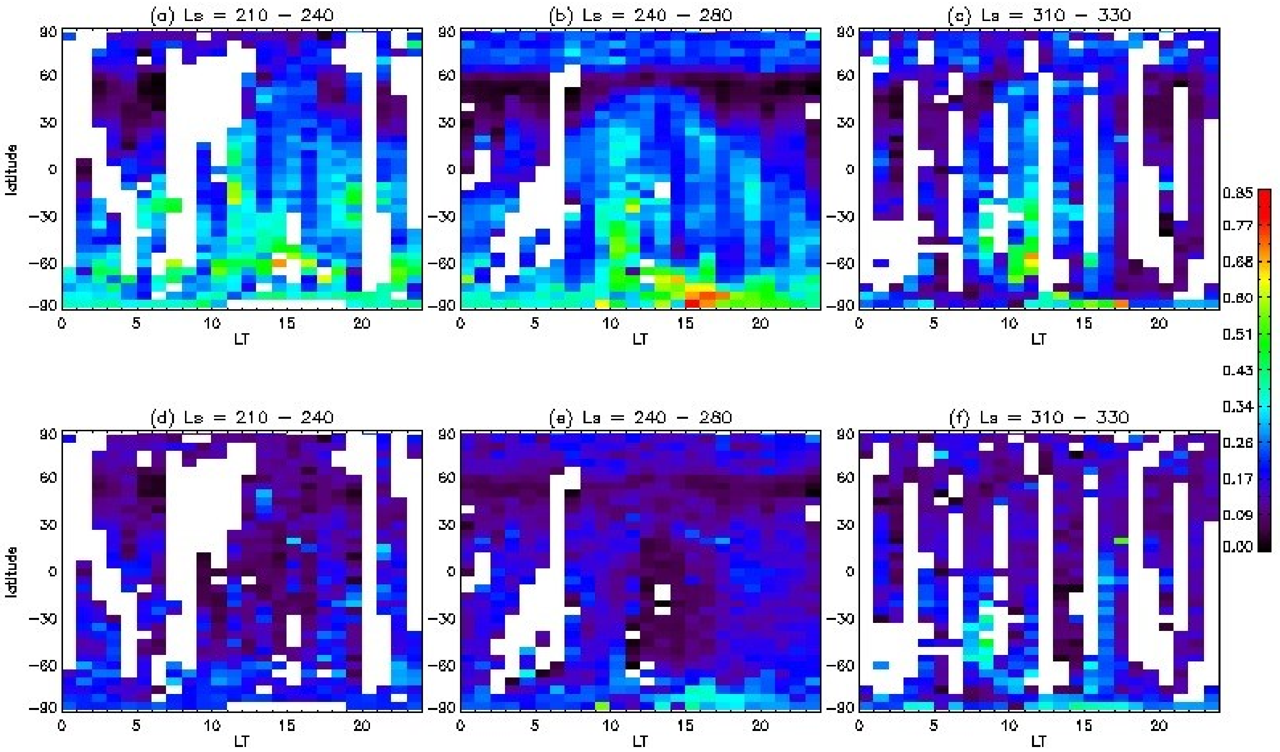

Fig.10. Dust opacity as a function of latitude and LT for specific Ls intervals corresponding to the duration of A (a), B (b) and C (c) storms. Standard deviations of dust opacity for each bin corresponding to the duration of A (d), B (e) and C (f) storms. We collected all MYs except for MY 28 and MY 34.

C storms are mainly constrained to southern latitudes in the L_s range from 310° to 330°. It occurs from the late morning to midday (**Fig. 10c**). However, again, dust is still active with opacity around 0.3 over northern mid-latitudes at 11 - 12 LT. In **Fig.1** in Kass et al. (2016) C storms are extended from the southern polar region to the equator. **Fig.10c** clearly shows the dusty atmosphere at 16 – 17 LT over the South Pole.

A clear atmosphere is recognized over northern high-latitudes around 60°N during the night in all panels of **Fig.10**. Kass et al. (2016) point out that atmospheric temperature increases in the high northern latitudes are the northern response to the atmospheric circulation. They exclude high dust loads which could induce the increase of atmospheric temperatures at 0.5 mbar.

We also investigated interannual variations of dust for A, B and C storms by plotting dust opacities as a function of LT for different years. A storms show some dust LT variations only for the northern hemisphere (**Fig.11a**), where the maximum of the dust opacity occurs at 11 LT in MY 29 as well as in MY 33. The dust opacity is elevated in MY 29 because of the regional dust storm and this is the year following the global dust storm. However, considering Fig.11a along with Fig.12a the peak at 11 LT in MY 29 in the northern hemisphere is due to the advancing season. A similar behavior is found in MY 33. Only two LTs (14 LT and 1 LT) are measured in the same day in MY 29 and they show a contrast in opacity. From 13 to 20 LT dust opacity is at around 0.2 - 0.25, and it is relatively large with respect to the other LTs during the night (0.1). After this detailed analysis, the A storms show only around twice the elevated dust opacities with respect to nighttime observations in the northern hemisphere. For the southern hemisphere there is no clear LT variation of dust opacity (**Fig.11b, 12b**). We observe the elevated dust opacity between 0.3 – 0.4. The similar dust behaviors over northern and southern hemispheres are shown in **Fig.10a**.

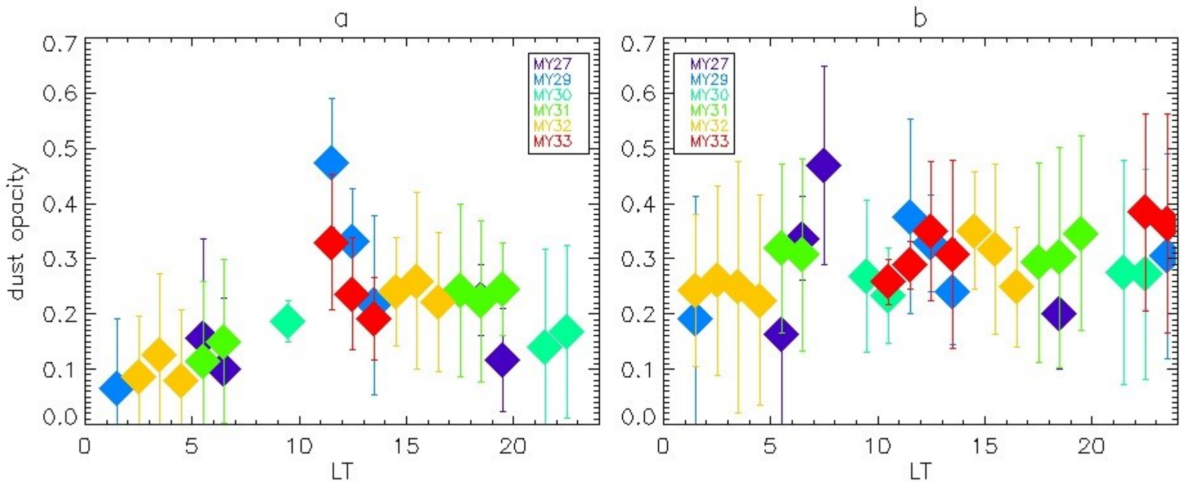

Fig. 11. Dust opacities as a function of LT for different MYs for A storms (a) 0 - 40°N, (b) 0 - 60°S.

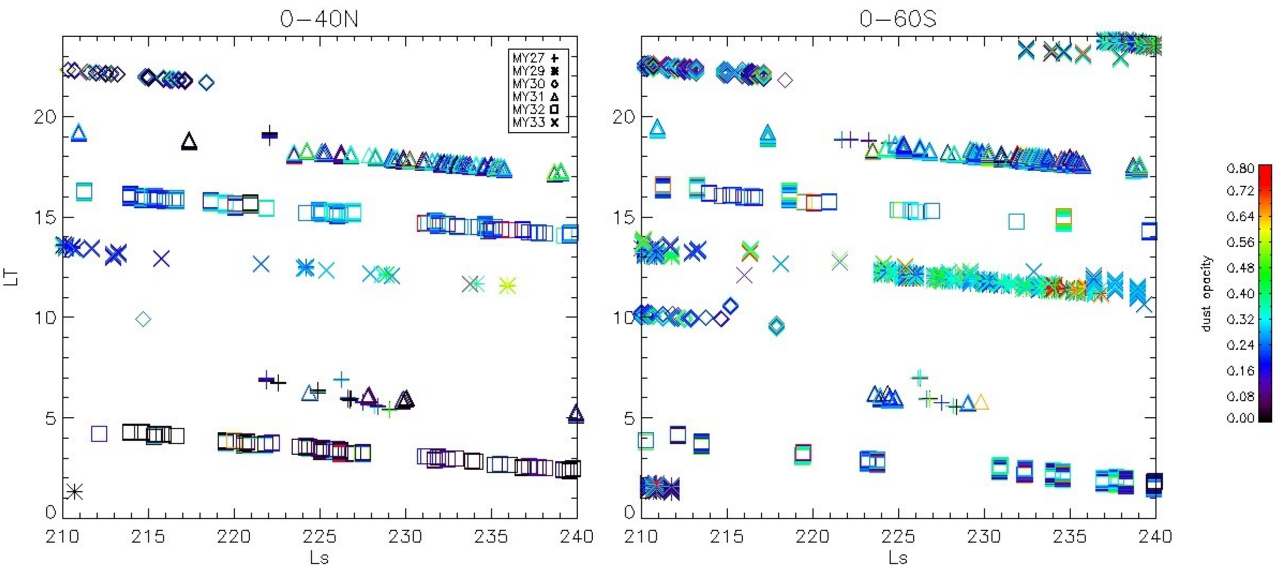

Fig.12. Dust opacities as a function of Ls and LT in different MYs during A storms for a) 0 - 40°N and b) 0 – 60°S. Different symbols correspond to different MYs and they are presented in the legend.

B storms “” have a particular behavior because a large dust activity occurs close to the South Pole and, thus we considered three regions separately: 1) from the equator to 40°N (northern hemisphere) (**Fig.13a**), 2) from the equator to 60°S (southern mid-latitudes) (**Fig.13b**) and 3) from 75°S to 90°S (South Pole) (**Fig.13c**). The maximum dust opacity is observed at 11 LT in MY 29 for the northern and southern hemispheres in “B” storms (**Fig.13a and 13b**). The spike in MY 29 B-storm activity at 11 LT shown in Figures 13a and 13b appears to be a hold-over from the relatively late A-season storm in that year. The decrease in opacity as local time moves to 8 LT is due to the advancing season. However, the difference in opacity between 11 LT and 21 – 22 LT is observed in the northern hemisphere as well as in the southern hemisphere for the same day in MY 29 (Fig.13a,b). A similar behavior for dust is also found in A storms in MY 29 and 33 (**Fig.11**). However, in B storms we found more inter-annual LT variation of dust than in A storms. **Fig.13b** shows the LT dust variation for the region from the equator to 60°S. The dust activity is different only in MY 29 in B storms with respect to other MYs. The LT variation of dust is within 0.15 to 0.35 except for MY 29. Again the dust opacity increase with LT in the morning in MY 29 is due to the advancing season. However, the regional storms in MY 29 show a large contrast between 11 LT and 23 LT observations. This difference in opacity resembles the activity of dust during global dust storms.

B storms over the South Pole are characterized by a peculiar behavior (**Fig.13c**). We observe the maximum of dust opacity in the afternoon from 15 LT in MY 33 to 20 LT in MY 30. This peak is present each Martian year except for MY 29 due to lack of data. The maximum is most pronounced at 15 LT in MY 32 and at 17 LT in MY 33. Less intense dust activity is found at 20 LT in MY 30 and elevated dust opacities (0.55) are observed from 17 LT to 21 LT in MY 31. A small peak during late afternoon (15 – 16 LT) is observed in MY 27. During the night there is no large year-to-year LT variation. The dust opacity oscillates around 0.4 (Fig.13c).

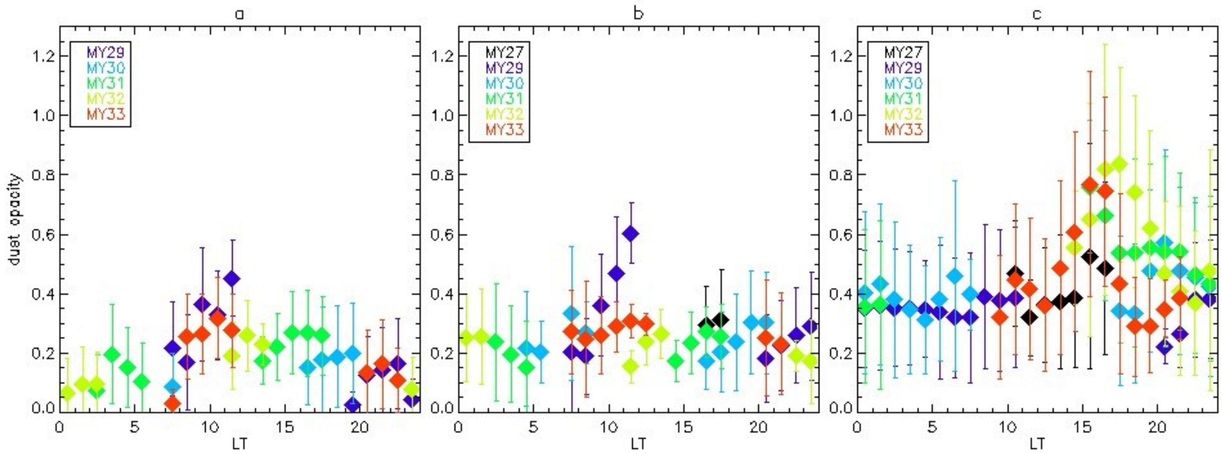

Fig.13. Dust opacities as a function of LT for different MYs for B storms (a) 0 - 40°N, (b) 0 - 60°S, (c) 75°S - 90°S.

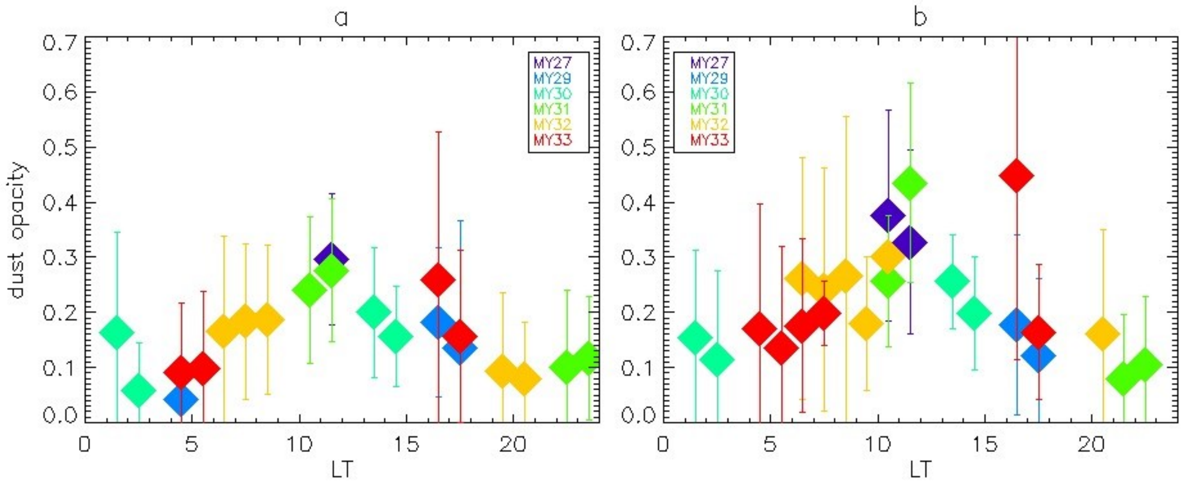

Fig.14. Dust opacities as a function of LT for different MYs for C storms (a) 0 - 40°N, (b) 0 - 55°S.

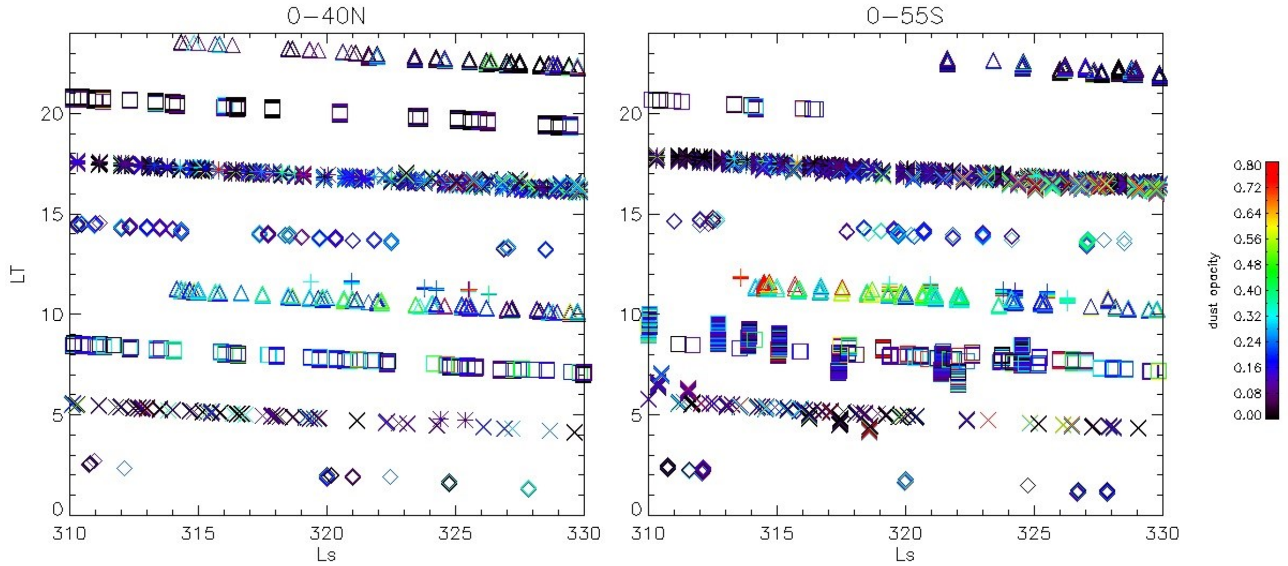

Fig.15. Dust opacity as a function of Ls and LT in different MYs for C storms a) 0 – 40°N and b) 0 - 55°S. Different symbols correspond with different MYs as in the legend of Fig. 12.

“C” storms have a similar behavior with LT for the northern and southern hemispheres (**Fig.14a and 14b**). The dust opacity peaks at 11 - 12 LT in MY 27 and MY 31 (Fig.15a,b). However, the dust opacity maximum at 11 - 12 LT is a true relative maximum only in MY 31 because the decrease of dust opacity is observed at 22 LT in the same day. In MY27, gaps occurred in the data. In MY 33, dust maximum is observed only at 16 LT for the northern as well as for the southern hemispheres. The decrease of dust opacity from 16 LT to 17 LT in MY 33 is due to the seasonal effect (Fig.15a,b). However, in both hemispheres a difference in afternoon (16 LT) and night dust opacities is observed for the same day in MY 33. This maximum at 16 LT is also observed in Fig.9a. In Fig.10c this maximum is not visible because all MYs except for MY 28 and 34 were used in the calculation of averages for each bin. Two measurements in MY 29 and MY 33 averaged at 16 LT give a mean value consistent with the value in Fig.10c. A similar peak was also observed in B storms at the southern polar region. At night, dust opacities have lower values down to 0.1 and less than 0.1 for the northern region.

With this analysis we found clear differences between dust opacities during day and night, especially for the northern hemisphere for all types of storms. Dust over the southern mid-latitudes shows a moderate and constant variation with LT with some inter-annual discrepancies. The most unusual behavior is found in B storms at the South Pole with maximum dust opacity observed in the afternoon (14 – 20 LT).

2.3. Dust activity in non-dusty season for all MYs

Northern springs and summers are characterized by small dust activity. Even in the year with the global dust storm (MY28) there is no special dust increase in these two seasons. In order to illustrate better a behavior of dust over the course of a 24-hour day, we selected the L_s range from 50° to 130°, on either side of the northern summer solstice. **Fig.16** presents the dust variation with LT for both hemispheres. We clearly observe that dust activity follows the sun respectively in both hemispheres.

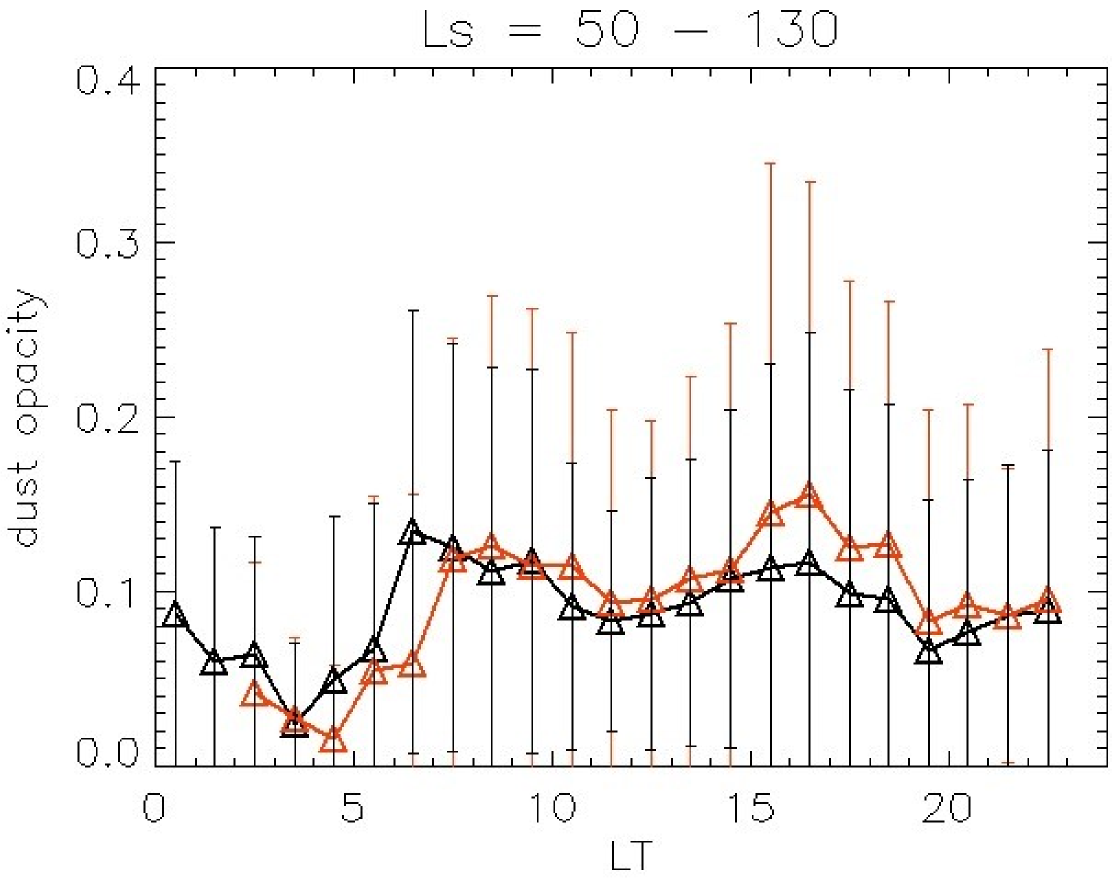

Fig.16. The dust variation with LT for Ls interval from 50° to 130° on either side of the northern summer solstice. Data binned with 1-hour bin and collected for the southern (0 - 25°S) and northern hemispheres (0 - 25°N) are plotted by red and black triangles, respectively. The “error bars” represent the standard deviation of each averaged value and provide an indication of the observed zonal, meridional, and inter-annual variations.

Sunrise, and with it dust increases, occur approximately one hour earlier in the northern than in the southern hemisphere. This is consistent with the northern summer solstice period when the sun insolation is greatest over northern mid-latitudes. There is a clear trend of dust opacity during the daytime, with two local maxima observed in the morning and in the late afternoon around 17 LT. The similar bimodal distribution of dust devil activity during daytime in the northern spring and summer can be reproduced by a model (Chapman et al., 2017). Maxima of dust devil activities are found at around 8 – 9 LT and in the afternoon at 15 – 17 LT, consistent with our results. The next specific behavior is characterized by a minimum atmospheric dust content, and is found during night/early morning. The minimum with respect to the daytime variation lasts longer during the night in the southern than in the northern hemisphere at this time at the year. The sun rises later for the southern hemisphere, leading to the longer night there. The variation of standard deviations is larger for the southern hemisphere than for the northern hemisphere. The nighttime behavior of dust with a minimum at 4 - 5 LT is strictly associated with the occurrence of water-ice clouds. Fig.12 in Hinson and Wilson (2004) shows the model LT variations of water-ice clouds and temperatures in the equatorial region during the aphelion season. Maximum activity of water-ice clouds was found from 23 – 8 LT, depending on altitudes, and this behavior illustrates the extent of control on clouds by tides (Hinson and Wilson, 2004).

In conclusion, during the non-dusty season we observe a different daily cycle of dust compared to the daily variation in the dusty season during global dust storms. The minimum of dust opacity is found during the early morning, then suddenly at around 6 – 7 LT dust content starts increasing threefold. Dust opacity increases faster in the northern hemisphere than in the southern hemisphere. During the daytime, the dust amount varies around the mean value (0.15) for this season with two small local maxima. After sunset it decreases gradually. These results are consistent with those obtained from the MCS MRO instrument describing the high altitude dust maximum (HATDM) over the tropics during the northern summer solstice (Heavens et al., 2011). They also found that the dust opacity increases threefold during the daytime compared to nighttime.

3. Discussion

During global dust storms we find a large daily variation of dust opacities (**Fig.5, 6, 7**). We analyzed the results in terms of capabilities in a retrieval of dust opacities in the vicinity 5 – 9 LT and 16 – 19 LT, when only a small contrast between atmospheric and surface temperatures should occur. This contrast undergoes a change in sign in the morning as surface temperatures climb above air temperatures (in the lower atmosphere) and again in the evening as the surface begins to cool down.

The impact of dust storm events is likely to make this issue more problematic, as nighttime surface temperatures are increased by increased downward IR flux from the warmed atmosphere, while daytime surface temperatures are decreased due to attenuated solar radiation. However, we found that for the considered latitude range from 40.5N to 40.5S, the contrast was not small. An isothermal atmosphere was absent in this region. We demonstrated this through a calculation of synthetic spectra for different dust opacities at three LTs (6.18, 18.81, 18.32). Dust had a large impact on spectra, which was clear in the dust absorption band (Appendix B, Fig.B1 and B2), especially when an atmospheric thermal inversion occurred. Thereby, we are confident in these retrievals of dust opacities even in the morning and in the evening, although they can have a large uncertainty as is shown in Fig.1b.

The difference in dust opacities found before midday and in the evening is large and can be associated with the presence of winds. Significant daily variation of a wind system (Goody and Belton, 1967; Gierasch and Goody, 1968) can lift the dust from the surface, possibly inducing the daily dust variations. Whether or not the surface wind stress plays a key role in the rapid increase of dust observed by PFS in the morning, the decrease of opacity consistently observed in the evening (early night) is even more puzzling. Once suspended, dust particles will slowly fall to the ground under the influence of gravity, as their density is greater than the atmospheric density. Settling velocity increases with particle size, with sedimentation timescales varying from hours for large particles to days and months for small particles, depending also on their altitude. Sedimentation is likely the main mechanism of dust deposition on the surface because scavenging by water ice is not very likely in the core of a global dust storm during daytime due to great atmospheric temperatures. Cantor et al. (2001) suggest that local dust storms that are observed to disappear within one diurnal cycle are probably composed of large particles, because coarse-grained particles will settle out of the Martian atmosphere very rapidly. The observed rapid variation of opacity with LT requires large dust particles to be lifted and deposited back to the surface each day in about ten hours.

The dust particles, depending on their size, are raised from the surface by saltation process, dust devils and surface winds (Cantor et al., 2001). The wind tunnel experiments conducted in the simulated Martian conditions allow the sufficient wind velocity to be estimated (Greeley et al., 1980). The required surface wind speed in order to lift particles with sizes around 100 μm, is around 50 m/s over a flat surface of erodible grains (Greeley et al., 1980). However, the meteorological data obtained from the sites of the Viking landers show that 25 – 30 m/s winds are able to raise grains with sizes from 10 – 100 μm (Greeley et al., 1980). Moreover, the wind tunnel experiment demonstrates that the threshold wind shear (friction wind speed) is minimal for particles with diameters of 80 – 100 μm in Martian conditions (Balme and Greeley, 2006). Thus these particles are most easily introduced into the atmosphere (Balme and Greeley, 2006). It also means that grains with smaller or larger sizes require stronger winds. Recently, wind tunnel experiments conducted under 0.38g (g - terrestrial acceleration) (Musiolik et al., 2018) show that the derived threshold wind shear velocity is lower than obtained in prior experiments (Greeley et al., 1980). As a result, the saltation of dust particles and their suspension are possible under Martian conditions at a lower threshold shear velocity (0.82 ± 0.04 m/s) (Musiolik et al., 2018) than originally estimated (1.5 – 2 m/s) by Greeley et al. (1980).

Cantor et al. (2001) suggest that large particles are involved in the diurnal variation of local dust storms because they have a tendency to be suspended in the atmosphere for a very short time. However, according to Cantor et al. (2001) the coarse-grained particles cannot be responsible for large local dust storms over the landing sites of the Viking rovers. Large particles undergo saltation but their trajectories are ballistic near the surface. Thus they are not able to soar to high altitudes. However, the impact of large particles on the ground induces the lifting of small particles. When the saltation process is repeated many times, finer dust particles are raised from the surface and are suspended in the atmosphere longer than coarse ones.

On the other hand, all grain sizes are involved in dust devils. The vortex threshold speed for such an injection appears to be relatively independent of particle size (Neubauer, 1966; Greeley et al., 1981; Cantor et al., 2001). Dust devils can extend as high as the convective boundary layer, that is on the order of 10 km (Mulholland et al., 2015; Chapman et al., 2017). Particles are lifted from the ground and enter in a vertical, upward-spiraling column of air (Chapman et al., 2017). Numerical simulations of the vertical transport in dust devils were performed by Gu et al. 2006; Spiga et al. 2016. They considered three sizes of grains (100, 200 and 300 μm). They point out that the small sized particles (100 μm) are lifted up and form a dust devil core. The others rotate around the core. After some time, the heaviest and the finest particles are found close to the surface and in the top of the core, respectively, leading to stratification (Gu et al., 2006; Spiga et al., 2016).

The dust devils shown by Viking orbiter images are roughly 100 – 1000 m wide and extend a few kilometers above surface (Ellehoj et al., 2010). Many dust devil tracks are found during southern summer seasons over Argyre and Hellas basins from MOC images (Balme et al., 2003). Thus, we anticipate that the dust particles with large grains might be lifted up to relatively high altitudes in many dust devils. However, at the moment, we know little about the processes that actually dominate in the extreme conditions of an on-going global dust storm. Other mechanisms could be established, such as enhanced tides, vertical transport and velocities, and possibly other unidentified mechanisms.

As a matter of fact, the current climate models are unable to reproduce the observed diurnal (and daily) variation in the dust content, even during the non-dusty season.

4. Summary and conclusions

We analyzed dust opacities obtained from PFS measurements from L_s = 331° of MY 26 until L_s = 300° of MY 34. We found three typical behaviors of dust opacities varying with LT depending on the season in the Martian year. We separated the data from MY 28 and MY 34 with the global dust storms, and from MY 29 with the regional storm from other MYs. We observed a striking behavior of dust opacities during these three years in the dusty seasons. Namely, we find large values of dust opacities at around 10 - 11 LT compared to the evening observations. The study of models of dust devil activity using MGCM (Mars Global Circulation Model) also predicts a peak before midday at many locations on Mars (Chapman et al., 2017). Large areas on Mars are involved in dust devil activity in the morning according to the MGCM (Chapman et al., 2017).

When surface stresses as a result of winds are strong enough, dust enters the Martian atmosphere (Haberle, 1986) by saltation and other means (Greeley et al., 1980). Some local dust storms can last about a day and can be of limited scale (around 10^4 km^2) (Haberle, 1986). During the global dust storms, large size particles can be lifted from the surface by increasing upward motions in the morning as an effect of growing insolation (Goody and Belton, 1967; Gierasch and Goody, 1968). Then after midday large particles of dust can deposit onto the surface very quickly, causing the dust opacity depletion in the atmosphere (Cantor et al., 2001). Significant dust opacities which are small with respect to the increase during the morning hours are then observed by PFS during the early evening (20 LT). Other processes such as a nucleation of water ice crystals can be involved in the sudden drop of dust content. Dust can be the nuclei for water-ice clouds and then it becomes transparent in attempts at its detection.

We also analyzed the behavior of dust opacities with LT in the dusty seasons of other MYs (typical Martian year). Elevated dust opacities are observed, but there is no significant variation with LT. In our results, with plots of zonally averaged dust opacities as a function of latitude and LT, we recognize three types of storms presented by Kass et al. (2016) and fully describe their variations with LT for the typical Martian year. We find that A storms are uniformly distributed with LT over the southern hemisphere during the whole nighttime and daytime. Elevated dust opacities are observed during afternoon hours compared to low values during the night in A storms in the northern hemisphere. B storms are clearly seen during late afternoon close to the South Pole. C storms show a more intense activity in the southern latitudes with respect to the northern hemisphere. Large dust opacities are found before midday (10 – 11 LT) compared to the evening/early night observations. C storms also have an exceptional second peak of activity at 16 LT in MY 33.

In the non-dusty seasons of other MYs, dust shows significant minima during late night and early morning compared to the variation during daytime. We observed at the northern summer solstice that the variation of dust opacities strictly follows the sun in the morning. Two small local maxima prominent in the morning and afternoon are similar to the daily dust devil activity described by Chapman et al. (2017). The low dust content is observed longer in the atmosphere over the southern than the northern hemisphere. Dust varies threefold between daytime and nighttime, consistent with results by MCS (Heavens et al., 2011) for this season.

Acknowledgments

This work has been performed under the UPWARDS project. This project has received funding from the European Union's Horizon 2020 research and innovation programme under grant agreement No633127. We also thank Michael Wolff and John Wilson for their insightful comments.

Appendix A

We analyzed an effect of different vertical dust profiles ('a priori') on a retrieval of column-integrated dust opacities. The different vertical dust profiles were derived from a dataset of coefficients provided by Nicholas Heavens based on the paper (Heavens et al., 2011). This dataset was built using the MCS data, namely, an analytical formula introduced by Heavens et al. 2011 was used to fit to the measured vertical dust extinction profile by the MCS. The vertical dust profiles were extended to the surface using the formula (eq.15) in Heavens et al. 2011. The vertical dust profiles built from the coefficients provided by N. Heavens were density scaled dust opacities. To simulate the effect of the different vertical dust profiles, we selected 7 PFS measurements from 7 different orbits. The analysis was performed for 6 different dust vertical profiles taken during day (corresponding with PFS orbits: 4328, 4428 and 4510) and night (corresponding with PFS orbits: 4867, 6562, 6568, 7346 (Fig.A1)). The same vertical dust profile was selected for two orbits: 6568 and 6562. All of these vertical dust distributions are the best guesses in latitudes and seasons for corresponding PFS orbits. These profiles were inserted as initial vertical dust profiles to our retrieval code.

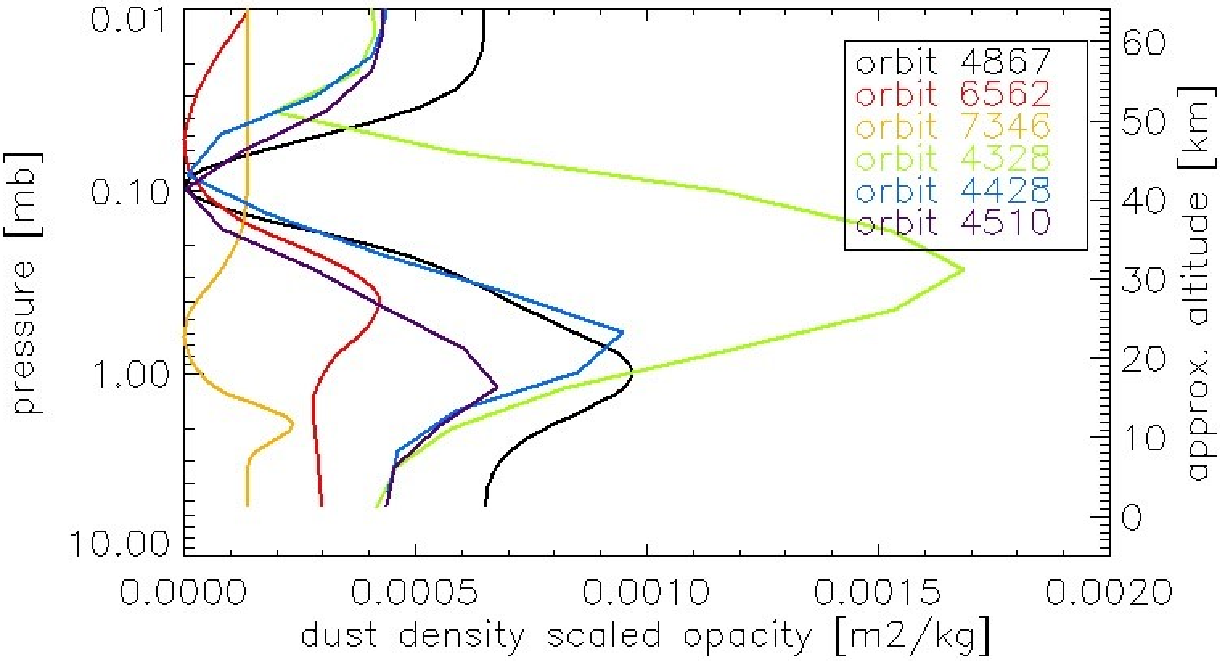

Fig.A1. Vertical dust distributions derived from fits to MCS data for a location and season of each PFS measurement.

For these vertical dust profiles (Fig.A1) we determined temperature profiles and column integrated dust optical depths. We compared then them with original temperature profiles and total dust optical depths based on initial vertical dust distributions taken from EMCD v.4.2 database, which were a function of exponential decrease.

Fig.A2 shows temperature profiles retrieved for 'MCS' dust profiles (dashed lines) and for dust profiles taken from EMCD v.4.2 (solid lines). We observe differences between temperature profiles for two orbits: 7346 and 4510. The temperature profile obtained from the measurement of orbit 7346 for the initial MCS vertical dust distribution shows the thermal inversion close to the surface (first 3 km) (dashed red line in Fig.A2). In the case of orbit 4510 we observe only ~ 1 K difference at ~20 km of altitude. In conclusion, we see no impact on temperature profiles. For the other measurements temperature profiles are consistent. The characteristic features of measurements are given in Tab. A1.

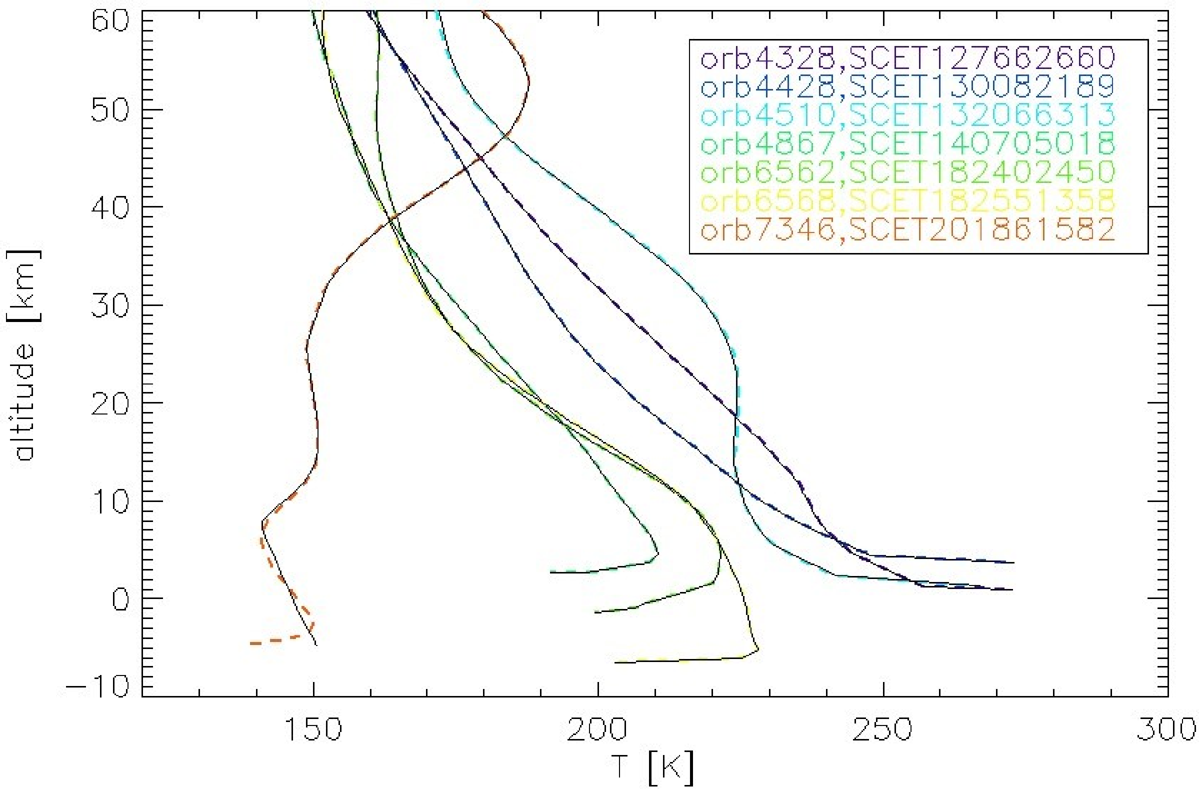

Fig.A2. Atmospheric temperatures for selected PFS measurements using initial vertical dust profiles from Fig.A1 (dashed lines) and original from EMCD 4.2 (solid line).

Table. A1. Characteristic features of measurements and calculated values of dust opacities for initial MCS vertical dust distributions and EMCD.

Number of orbit	Ls	LT	Latitude	Longitude (-180E;180E)	Dust opacity (MCS)	Dust opacity (EMCD)	Surface temperature (MCS)	Surface temperature (EMCD)
4328	241	14.22	40.13S	-3.04 E	0.414	0.412	296.8	296.632
4428	259	12.82	34.08S	-111.18 E	0.163	0.162	301.385	301.339
4510	273	12.13	27.46S	116.91 E	1.527	1.727	248.855	249.94
4867	332	5.76	23.25S	-79.84 E	0.186	0.184	189.522	189.474
6562	208	1.82	47.31S	-53.24 E	0.212	0.212	198.848	198.822
6568	209	1.74	45.96S	61.72 E	0.775	0.767	198.55	198.573
7346	343	3.76	66.93N	-71.7 E	0.191	0.188	147.948	147.955

A small variation of total dust opacity is found for orbit 4510 when high dust loading occurs. The difference is ~12% with respect to the original version (Tab. A1). Most of the dust opacity variations due to location and season are larger than this difference for high dust loadings (during global dust storms), for example Fig.4. For the other orbits, the difference between results is ~1% even for a medium dust opacity (orbit 6568). On this basis, the dust opacity uncertainty due to unknown vertical dust distribution can be estimated for ~10%.

Appendix B

An impact of different dust opacities on spectra at three LTs (in the morning and in the evening) is presented in Fig.B1. The smallest differences between spectra calculated for the different dust opacities are observed for the measurement taken at 6.18 LT (SCET number 303336673).

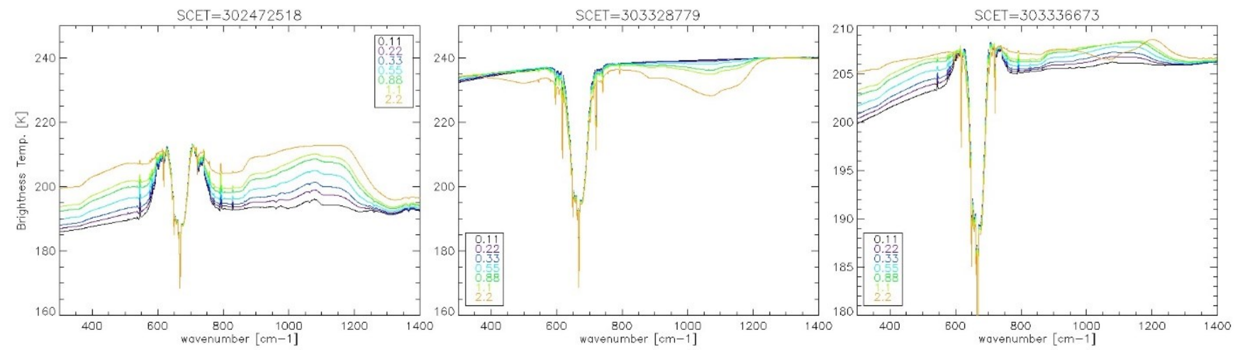

Fig.B1. Model spectra calculated for three different temperature profiles (at three LTs: 6.18, 18.81, 18.32) presented in Fig.B2 and for different dust opacities shown in the legend.

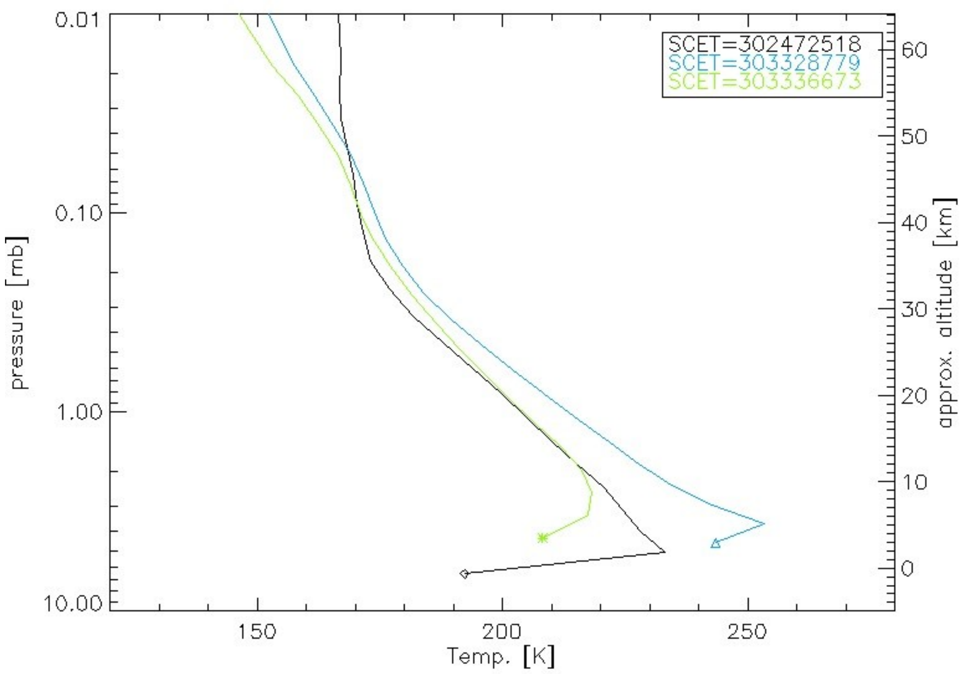

Fig.B2. Temperature profiles extracted from EMCD v5.3 for atmospheric conditions similar to three PFS measurements in MY31. Black line corresponds to the PFS measurement (SCET 302472518) taken at 18.81 LT, Ls = 217.38, latitude 16.77N and longitude 15.52E. Blue line corresponds to the PFS measurement (SCET 303328779) taken at 18.32 LT, Ls = 223.52, latitude 28.18S and longitude 136.69E. Green line corresponds to the PFS measurement (SCET 303336673) taken at 6.18 LT, Ls = 223.58, latitude 28.6S and longitude -73.14E. Symbols mean surface temperatures for each measurement.

References

Balme, M. R., P. L. Whelley, and R. Greeley, (2003), Mars: Dust devil track survey in Argyre Planitia and Hellas Basin, *J. Geophys. Res.*, 108(E8), 5086, doi:10.1029/2003JE002096.

Balme, M. and R. Greeley, (2006), Dust devils on Earth and Mars, Rev. Geophys., 44, RG3003, doi:10.1029/2005RG000188.

Cantor B. A., P. B. James, M. Caplinger and M. J. Wolff, (2001), Martian dust storms: 1999 Mars Orbiter Camera observations, *J. Geophys. Res.*, vol. 106, No. E10, 23,653 – 23, 687.

Chapman R.M., S.R. Lewis, M. Balme, L.J. Steele, (2017), Diurnal variation in martian dust devil activity, Icarus, 292, 154 – 167, https://doi.org/10.1016/j.icarus.2017.01.003.

Clancy, R. T., A. W. Grossman, M. J. Wolff, P. B. James, D. J. Rudy, Y. N. Billawala, B. J. Sandor, S. W. Lee., and D. O. Muhleman, (1996). Water vapor saturation at low altitudes around Mars aphelion: A key to Mars climate? *Icarus,* 122, 36–62.

Davies D.W., (1979), Effects of Dust on the Heating of Mars' Surface and Atmosphere, *J. Geophys. Res.*, vol. 84, No. B14, 8289 – 8293.

M. D. Ellehoj, H. P. Gunnlaugsson, P. A. Taylor, H. Kahanpää, K. M. Bean, B. A. Cantor, B. T. Gheynani, L. Drube, D. Fisher, A.-M. Harri, C. Holstein-Rathlou, M. T. Lemmon, M. B. Madsen, M. C. Malin, J. Polkko, P. H. Smith, L. K. Tamppari, W. Weng, and J. Whiteway, (2010), Convective vortices and dust devils at the Phoenix Mars mission landing site, *J. Geophys. Res.*, vol. 115, No. E00E16, doi:10.1029/2009JE003413.

Fenton L. K., J. C. Pearl and T. Z. Martin, (1997). Mapping Mariner 9 Dust Opacities, *Icarus,* 130**,** 115–124.

Forget, F., et al., (1999a), Improved General Circulation Models of the Martian Atmosphere from the Surface to above 80 km, *J. Geophys. Res.*, 104, (E10), 24155-24176.

Forget, F., et al., (1999b), A Climate Database for Mars, *J. Geophys. Res.*, 104, (E10), 24177-24194.

Giuranna M., P. Wolkenberg, D. Grassi, A. Aronica, S. Aoki, D. Scaccabarozzi, B. Saggin, V. Formisano, (2019), The current weather and climate of Mars: 12 years of atmospheric monitoring by the Planetary Fourier Spectrometer on Mars Express, Icarus, https://doi.org/10.1016/j.icarus.2019.113406.

Grassi, D., Ignatiev, N.I., Zasova, L.V., Maturilli, A., Formisano, V., Bianchini, G.A., Giuranna, M., (2005), Methods for the analysis of data from the Planetary Fourier Spectrometer on the Mars Express mission. Planet. Space Sci. 53 (10), 1017–1034.

Greeley, R., R. Leach, B. White, J. Iversen, and J. Pollock, (1980). Threshold wind speeds for sand on Mars: Wind tunnel simulations, Geophys. Res. Lett., 7, 121-124.

Greeley, R., B. R. White. J. B. Pollack, J. B. Iversen, and R. N. Leach (1981), Dust storms on Mars: Considerations and simulations, Spec. Pap. Geol. Soc. Am., 186, 101-121.

Gierasch P. and R. Goody, (1968). A study of the thermal and dynamical structure of the Martian lower atmosphere, *Planet. Space Sci.*, vol. 16, pp. 615 – 646.

Goody R. and M. J. S. Belton (1967). Radiative relaxation times for Mars, a discussion of Martian atmospheric dynamics, *Planet. Space Sci.*, vol. 15, pp. 247 – 256.

Gu Z., Y. Zhao, Y. Li, Y. Yu, and X. Feng, (2006). Numerical Simulation of Dust Lifting within Dust Devils – Simulation of an Intense Vortex, Journal of Atmospheric Sciences, 63, 2630 – 2641.

Haberle, R.M., (1986), Interannual variability of global dust storms on Mars, *Science*, 234, 459-61.

Hanel, R., B. Conrath, W. Hovis, V. Kunde, P. Lowman, W. Maguire, J. Pearl, J. Pirraglia, C. Prabhakara, and B. Schlachman (1972). Investigation of the martian environment by infrared spectroscopy on Mariner 9. *Icarus* 17, 423–442.

Heavens, N. G., M. I. Richardson, A. Kleinböhl, D. M. Kass, D. J. McCleese, W. Abdou, J. L. Benson, J. T. Schofield, J. H. Shirley, and P. M. Wolkenberg (2011a), Vertical distribution of dust in the Martian atmosphere during northern spring and summer: High-altitude tropical dust maximum at northern summer solstice, J. Geophys. Res., 116, E01007, doi:10.1029/2010JE003692.

Heavens, N. G., M. S. Johnson, W.A. Abdou, D.M. Kass, A. Kleinböhl, D. J. McCleese, J. H. Shirley, and R. J. Wilson (2014), Seasonal and diurnal variability of detached dust layers in the tropical Martian atmosphere, J. Geophys. Res. Planets, 119, 1748–1774, doi:10.1002/2014JE004619.

Hinson, D., and R.J. Wilson, 2004: Temperature inversions, thermal tides, and water ice clouds in the martian tropics, *J. Geophys. Res.*, 109, E01002, doi:10.1029/JE002129.

Kass, D. M., A. Kleinböhl, D. J. M cCleese, J. T. Schofield, and M. D. Smith (2016), Interannual similarity in the Martian atmosphere during the dust storm season, *Geophys. Res. Lett.*, 43, 6111–6118, doi:10.1002/2016GL068978.

Kleinböhl A., A., Spiga, A., Kass, D. M., Shirley, J. H., Millour, E., Montabone, L., & Forget, F. (2020). Diurnal variations of dust during the 2018 global dust storm observed by the Mars Climate Sounder. *Journal of Geophysical Research: Planets*, *125*, e2019JE006115. https://doi.org/10.1029/2019JE006115

Leovy C. B., J. E. Tillman, W. R. Guest, J. R. Barnes, Recent Advances in Planetary Meteorology, G. E. Hunt, Ed. (Cambridge Univ. Press, Cambridge, 1985), pp. 69 – 84.

Leovy, C. B. 1985. The general circulation of Mars: Models and observations, *Adv. Geophys.* 28a, 327–346.

Martin, T. Z., and H. Kieffer, (1979). Thermal infrared properties of the martian atmosphere, 2: The 15 µm band measurements. *J. Geophys. Res.* 84, 2843–2852.

Martin T. Z., A. R. Peterfreund, E. D. Miner, H. H. Kieffer and G. E. Hunt (1979), Thermal Infrared Properties of the Martian Atmosphere 1. Global Behavior at 7, 9, 11, and 20 μm, *Journal of Geophysical Research*, vol. 84, NO. B6, 2830.

Martin T. Z., L. K. Tamppari, Diurnal variation of Martian dust opacity (2007), The seventh international conference on Mars, Pasadena, California, abstract, No. 3079.

Määttänen Anni, Constantino Listowski, Franck Montmessin, Luca Maltagliati, Aurélie Reberac, Lilian Joly, Jean-Loup Bertaux, A complete climatology of the aerosol vertical distribution on Mars from MEx/SPICAM UV solar occultations (2013), *Icarus*, 223, 892 – 941, http://dx.doi.org/10.1016/j.icarus.2012.12.001.

McCleese, D. J., N. G. Heavens, J. T. Schofield, W. A. Abdou, J. L. Bandfield, S. B. Calcutt, P. G. J. Irwin, D. M. Kass, A. Kleinbohl, S. R. Lewis, D. A. Paige, P. L. Read, M. I. Richardson, J. H. Shirley, F. W. Taylor, N. Teanby and R. W. Zurek (2010), Structure and dynamics of the Martian lower and middle atmosphere as observed by the Mars Climate Sounder: Seasonal variations in zonal mean temperature, dust and water ice aerosols, *J. Geophys. Res.*, 115, E12016, doi:10.1029/2010JE003677.

Millour, E., F. Forget, A. Spiga, T. Navarro, J.-B. Madeleine, L. Montabone, A. Pottier, F. Lefèvre, F. Montmessin, J. Y. Chaufray, M. A. Lopez-Valverde, F. Gonzalez-Galindo, S. R. Lewis, P. L. Read, J. P. Huot, M. C. Desjean add MCD/GCM development Team (2015), The Mars Climate Database (MCD version 5.2), European Planetary Science Congress 2015, held 27 September – 2 October, 2015 in Nantes, FranceAbstract 10: EPSC2015-438.

Mulholland D. P., P. L Read, S. R. Lewis (2013), Simulating the interannual variability of major dust storms on Mars using variable lifting thresholds, Icarus, 223, 344 – 358.

Mulholland D. P., A. Spiga, C. Listowski, P. L. Read (2015), An assessment of the impact of local processes on dust lifting in Martian climate models, Icarus, 252, 212 – 227.

Murphy, J.R., Toon, O.B., Haberle, R.M., Pollack, J.B., (1990), Numerical simulations of the decay of Martian global dust storms, *J. Geophys. Res.,* 95 (B9), 14629–14648.

Musiolik G., M. Kruss, T. Demirci, B. Schrinski, J. Teiser, F. Daerden, M. D. Smith, L. Neary, G. Wurm, (2018), Saltation under Martian gravity and its influence on the global dust distribution, *Icarus*, 306, 25-31.

Newman, C.E., S. R. Lewis, P. L. Read, and F. Forget (2002), Modeling the Martian dust cycle, 1. Representations of dust transport processes, J. Geophys. Res. (Planets), 107: E12, 5123.

Neubauer, F. M. (1966), Thermal convection in the Martian atmosphere, J. Geophys. Res., 71, 2419-2426.

Santee M. and Crisp D., (1993), Thermal Structure and Dust Loading of the Martian Atmosphere During Late Southern Summer: Mariner 9 Revisited, *J. Geophys. Res.,* 98 (E2), 3261-3279.

Smith M. D., (2004), Interannual Variability in TES Atmospheric Observations of Mars During 1999-2003, *Icarus*, 167, 148-165.

Smith M. D., (2009), THEMIS observations of Mars aerosol optical depth from 2002 – 2008, *Icarus*, 202, 444 – 452.

Spiga A., E. Barth, Z. Gu, F. Hoffmann, Junshi Ito, B. Jemmett-Smith, M. Klose, S. Nishizawa, S. Raasch, S. Rafkin, T. Takemi, D. Tyler, W. Wei, (2016). Large-Eddy Simulations of Dust Devils and Convective Vortices, Space Science Review, 203: 245, DOI 10.1007/s11214-016-0284-x.

Wilson R. J. and M. I. Richardson, (2000), The Martian Atmosphere During the Viking Mission, I, Infrared Measurements of Atmospheric Temperatures Revisited, Icarus, 145, 555-579, doi:10.1006/icar.2000.6378

Wolkenberg P., M. Giuranna, D. Grassi, A. Aronica, S. Aoki, D. Scaccabarozzi, B. Saggin, Characterization of dust activity on Mars from MY27 to MY32 by PFS-MEX observations (2018), *Icarus*, 310, 32 – 47, doi:10.1016/j.icarus.2017.10.045.

Zasova L. and Formisano V., Seasonal variation of temperature structure and aerosol in Martian atmosphere from PFS MEX data (2007), EPSC Abstracts, Vol. 2, EPSC2007-A-00434.

Zurek, R. W., J. R. Barnes, R. M. Haberle, J. B. Pollack, J. E. Tillman, and C. B. Leovy (1992), Dynamics of the atmosphere of Mars, in Mars, edited by H. H. Kieffer et al., pp. 835–933, Univ. of Ariz. Press, Tucson.